# SLM-Printed EUROFER Steel for Fusion Applications

Ramil Gaisin*, Carsten Bonnekoh, Simon Bonk, Heiko Neuberger, Vladimir Chakin, Michael Rieth

*Karlsruhe Institute of Technology, Kaiserstraße 12, 76131 Karlsruhe, Germany*

**Abstract**

This study investigates selective laser melting (SLM) of atomized EUROFER97 powder for fusion applications, focusing on two fabrications and their resulting microstructure, tensile properties, impact toughness, and leak-tightness. Optimized powder preparation improved chemical composition and grain size after heat treatment, enhancing Charpy impact toughness with an upper shelf energy surpassing the EUROFER97 standard and a lower ductile-to-brittle transition temperature (-120°C vs. -100°C). Tensile properties, including yield and ultimate strength and elongation, were similar to the EUROFER97 reference material.
SLM-printed capsules demonstrated excellent leak-tightness, with helium leak rates well below ITER requirements, and burst tests confirmed ultimate strengths exceeding 700 MPa. These findings showcase potential of SLM for creating complex components for fusion reactor blankets with tailored mechanical properties.

**Keywords:** EUROFER97; Additive manufacturing; Selective laser melting; Mechanical properties.

* Corresponding author

## 1. Introduction

Selective Laser Melting (SLM) is one of the most extensively studied additive manufacturing methods, where a high-powered laser selectively melts layers of metal powder to build complex structures layer by layer [1,2]. Each layer is melted in a predefined pattern, and upon solidification, forms a precise three-dimensional object with a high degree of geometric accuracy. This method has been successfully applied to a wide range of materials, including metals, ceramics [3], and composites [4], and offers significant advantages in fabricating complicated geometries that are challenging or impossible to produce using conventional manufacturing techniques. The application of SLM for producing components for future fusion reactors presents a unique opportunity. Potential applications include fabricating small, intricate components, such as tubes with thin internal channels or concentric pins, without the need for welding in Helium-Cooled Pebble Bed and Water-cooled Lead Ceramic Breeder blanket designs [5–7]. Another opportunity is to accelerate prototyping and material development, allowing for the rapid production of conventionally challenging components for testing, as well as the fabrication of small-scale samples with slight variations in chemical composition, significantly reducing time and material requirements. EUROFER97, a reduced-activation ferritic-martensitic steel, is a critical material for such fusion applications due to its excellent mechanical properties under neutron irradiation [8–12]. While EUROFER97 has been considered for SLM printing [6,7], its use for fusion-relevant applications is still in the early stages of development.

In a previous study [13], SLM was successfully employed to print blocks from atomized EUROFER97 powder. Despite the initial coarse microstructure of the printed material, subsequent standard heat treatment for EUROFER97 significantly refined the microstructure, resulting in tensile properties that were similar to the EUROFER97 specification [12], irrespective of the printing orientation. However, one critical limitation was identified: Charpy impact tests on specimens cut from the printed blocks revealed that the upper shelf energy (USE) was reduced to 40–70%, and the ductile-to-brittle transition temperature (DBTT) was shifted to a range between -50°C and +80°C, which could limit its applicability in fusion environments. This limitation motivated further investigations and, in particular, the use of a slightly different atomization route provided by a different company.

In this study, as a logical continuation of the previous work, new blocks were printed using a different batch of atomized EUROFER97 powder. The research compares the microstructure and properties of this new fabrication with the previous one. The primary focus of the investigation is on Charpy impact tests as well as the evaluation of printed capsules for helium leak tightness and burst properties. These results aim to further establish the feasibility of using SLM-printed EUROFER for fusion-relevant applications and address the limitations observed in prior studies.

## 2. Materials and experimental techniques

The starting material used was a powder with an average particle size of approximately 30 µm, produced by NANOVAL GmbH, Germany through the atomization of various EUROFER97 steel plates with continuous control of the melt mass flow and argon gas flow. The EUROFER97 plates used for atomization in Fabrication 2 originated from a different batch than those used in Fabrication 1, contributing to variations in the chemical composition of the resulting powders. Due to the relatively high volatility of chromium and the potential reduction in its content in the

resulting powder, a small amount of pure chromium was added during atomization to maintain the desired composition. Note that in the previous work, atomization was performed by a different company (Rosswag Engineering) using a boron nitride nozzle [13,14].

The 3D printing of the materials studied in this work was conducted at Rosswag GmbH, Germany, following the same technology outlined in a previous study [13,14]. Selective laser melting was carried out using an SLM280HL Twin machine from SLM Solutions. Printing parameters were selected based on prior research, with a layer thickness of 30 µm, hatch distance (spacing between scan lines) of 80 µm, scan speed of 0.8 m/s, and laser power of 200 W.

Twenty blocks (dimensions $40 \times 40 \times 10$ mm$^3$) and twenty capsules for leak and burst tests were fabricated using SLM. The build direction of blocks was vertical and aligned with the shortest side of the block (10 mm), as illustrated in Fig. 1. The capsules were fabricated using the same material and process parameters. The capsules were cylindrical, with a length of 56 mm, wall thicknesses of 0.5 mm, 0.7 mm, and 0.9 mm, and a build direction parallel to the longitudinal axis. Blocks and capsules underwent high-temperature hot isostatic pressing (HIP) in an argon atmosphere, performed by Bodycote, Germany. The processing conditions varied as they were part of different HIP campaigns: the blocks were treated at 1000°C for 2.5 h at 100 MPa, while the capsules underwent HIP at 1150°C for 4 h at 100 MPa. The difference in HIP parameters resulted from the fact that the blocks and capsules were processed in separate campaigns with different experimental timelines. Although the capsules were treated at a higher temperature and for a longer duration, the resulting microstructure after final heat treatment was similar to that of the blocks. Conventiona heat treatment for EUROFER97 was then applied, including heating to 980°C with a one-hour hold, followed by air cooling and annealing at 750°C for two hours, also followed by air cooling [12,15]. The heat treatment was conducted in a vacuum furnace. The entire vacuum tube containing the sample was subjected to air cooling, ensuring that the sample itself remained under vacuum conditions to prevent corrosion.

Tensile tests were conducted using the same type of flat specimens as in previous study [13], with a gauge length of 13 mm and a cross-section of $2 \times 1$ mm$^2$. Fig. 1a schematically illustrates the cutting of tensile specimens from the printed blocks. Some specimens were oriented with their flat surface parallel to the print plane (Orientation A), while others were oriented perpendicular to the build direction (Orientation B). The tests were performed at temperatures of 20°C, 300°C, 500°C, and 700°C in vacuum with an initial strain rate of $3 \times 10^{-4}$ s$^{-1}$, using a Zwick Z30 universal testing machine. For each temperature and orientation, three tensile specimens were tested, resulting in a total of 24 tests.

(a) (b)

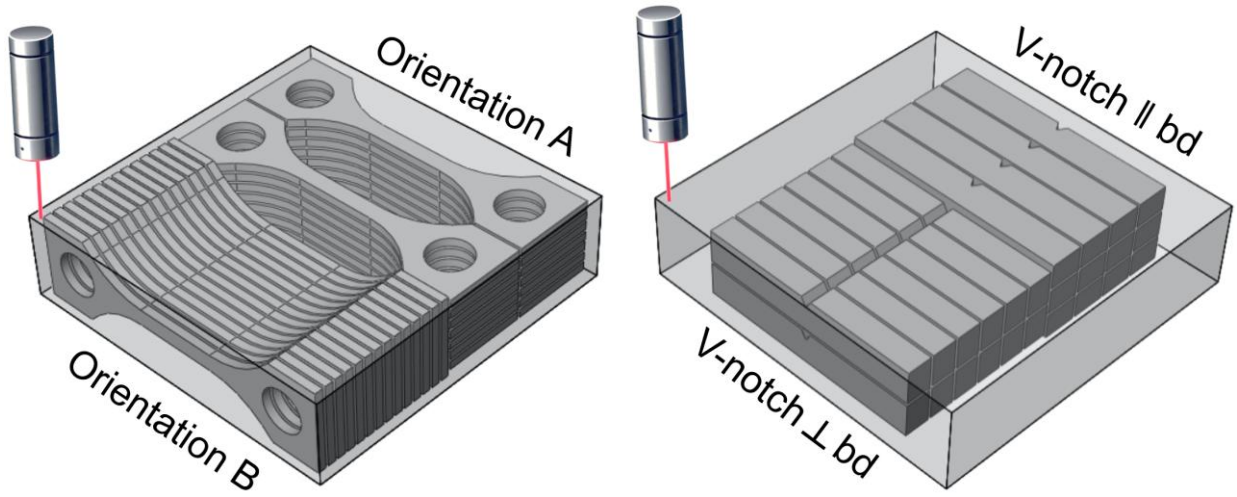


Fig. 1. Schematic of specimens cutting for (a) tensile and (b) Charpy impact tests

For the Charpy impact tests, sub-sized Charpy V-notch specimens (KLST) measuring 27 × 4 × 3 $mm^3$ were used. Fig. 1b also presents the cutting scheme for Charpy impact test specimens, where some specimens were extracted with the V-notch parallel to the build direction and others with the V-notch perpendicular to it. The tests were conducted at temperatures ranging from -150°C to 0°C on a Zwick machine with a pendulum energy of 27 J. In total, 12 Charpy specimens were tested for each orientation, with 1–2 specimens for each temperature point. All tensile and Charpy specimens were surface-ground to remove any surface defects and ensure consistent surface quality. No additional polishing was performed.

The capsules were tested for helium leak-tightness in a dedicated vacuum chamber by filling them with helium gas pressurized to 80 bar for 30 minutes, while a detector measured leakage rates. Burst strength was evaluated at room temperature by gradually filling the capsules with water at a rate of 1 bar per second until rupture occurred. The maximum pressure prior to failure was recorded to calculate the ultimate strength.

Microstructural studies were performed using scanning electron microscope (SEM) Zeiss Merlin. The chemical composition was evaluated using energy-dispersive X-ray spectroscopy (EDS). Electron backscatter diffraction (EBSD) was used to build surface normal-projected inverse pole figure (IPF-Z) orientation maps. The black and white lines on the maps indicate high- and low-angle grain boundaries, respectively. The reported grain size refers to the average spacing between high-angle grain boundaries (HAGBs), serving as an approximation of martensite lath packet size. No reconstruction of prior austenite grains (PAG) was performed.

Chemical composition was analyzed for both the powders and the corresponding SLM-printed samples of each fabrication using inductively coupled plasma optical emission spectrometry method (ICP-OES). The amount of argon was measured using a mass spectrometer with helium as the carrier gas during melt extraction (Swerim AB, Sweden). Vickers microhardness was measured using a Zwick Roell Indentec ZHμ tester with an indentation load of 1 kgf (HV1). For each sample and orientation, five indentations were performed and averaged. Density was measured by the hydrostatic weighing in $C_{14}H_{30}$ liquid medium (Mettler Toledo MS303TS) on samples after HIP and heat treatment.

## 3. Results and discussion

### 3.1. SLM-printed blocks

Fig. 2 shows the appearance of 3D-printed steel blocks with a composition close to EUROFER97 RAFM steel, produced via selective laser melting (hereafter referred to as SLM-EF Fabrication 2). These blocks are monolithic, solid parallelepipeds similar to those described for SLM-EF Fabrication 1 in [13]. The as-printed surface has a gray, matte finish with visible printing marks along the diagonal of the larger face. The measured density of the blocks was 7.787 g/cm³, differing from the density of Fabrication 1 blocks and EUROFER97 only within the margin of measurement error (7.744 g/cm³ [16]).

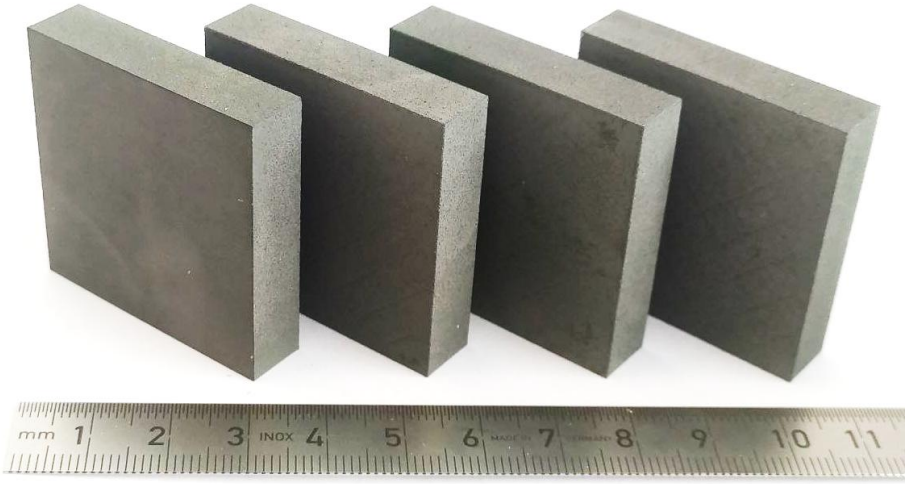


Fig. 2. Appearance of the as-received SLM-EF blocks, Fabrication 2 (40×40×10 $mm^3$), produced via selective laser melting

Table 1 presents the chemical composition of powders and the corresponding SLM-EF for Fabrication 1 and 2, compared to the EUROFER97 standard as the reference material and the specified standard. The table shows variations in the chemical composition of both the powder and printed products between Fabrication 1 and Fabrication 2, which can be attributed to the use of different EUROFER97 plates and distinct powder atomization methods. Specifically, differences in the initial concentrations of C, Mn, V, Ta, and Mo in the raw materials resulted in corresponding variations in the powders, while discrepancies in other elements, particularly O and B, were primarily due to the differences in the atomization process. For Fabrication 2, the carbon content in the powder is below the specified standard for EUROFER97, with a further reduction observed during the SLM process. It should be noted that the lower carbon content in Fabrication 2 could influence carbide precipitation and may affect long-term properties such as creep resistance. This aspect will be addressed in future studies. The manganese content in Fabrication 2 is nearly ten times higher than in Fabrication 1, although it remains below the minimum requirement of 0.2% according to the standard. The vanadium content in Fabrication 2 was reduced by approximately half and now complies with the standard.

Table 1. Chemical composition of SLM-EF (Fabrication 1 and 2) compared to the reference material EUROFER97 (EF_ref) and the specified standard (EF_spec) [13]. For powder atomization, different EUROFER97 plates with slightly varying compositions, compared to EF_ref, were used. Deviations from the standard element content are highlighted in bold text.

| Element, wt.% | SLM-EF | | | | EUROFER97 | |
|---|---|---|---|---|---|---|
| | Fabrication 1 | | Fabrication 2 | | EF_ref | EF_spec |
| | Powder | 3D-printed | Powder | 3D-printed | | |
| Cr | 9.46 | 9.39 | **9.61** | 9.37 | 9.36 | 8.5–9.5 |
| C | 0.1 | 0.09 | **0.0785** | **0.062** | 0.095 | 0.09–0.12 |
| Mn | **0.021** | **0.019** | **0.185** | **0.175** | 0.5 | 0.2–0.6 |
| V | **0.35** | **0.36** | 0.222 | 0.223 | 0.19 | 0.15–0.25 |
| N | 0.025 | 0.025 | 0.0245 | 0.0223 | 0.041 | 0.015–0.045 |
| W | 1.1 | 1.12 | 1.123 | 1.16 | 1.21 | 1.0–1.2 |
| Ta | 0.093 | 0.094 | 0.0612 | 0.059 | 0.1 | 0.05–0.09 |
| O | **0.022** | **0.0065** | **0.0302** | **0.0178** | 0.0103 | <0.01 |
| Si | 0.039 | 0.039 | 0.0404 | 0.042 | 0.033 | <0.05 |
| S | 0.002 | 0.002 | 0.0024 | 0.002 | 0.0017 | <0.005 |
| B | **0.0175** | **0.017** | 0.0004 | <0.0003 | - | <0.001 |
| Ti | 0.0002 | 0.0002 | 0.00024 | 0.00028 | 0.0008 | <0.01 |
| Nb | 0.0002 | 0.0005 | 0.0005 | <0.0005 | 0.0003 | <0.001 |
| Mo | 0.0014 | 0.0024 | 0.0099 | 0.0101 | 0.0024 | <0.005 |
| Ni | **0.0058** | **0.0094** | **0.0072** | **0.0076** | 0.0067 | <0.005 |
| Cu | **0.0097** | **0.011** | **0.0077** | **0.0075** | 0.007 | <0.005 |
| Al | **0.0037** | **0.0034** | 0.0009 | 0.0009 | <0.001 | <0.01 |
| Co | 0.0015 | 0.0016 | 0.0042 | 0.0044 | - | <0.005 |

Due to the characteristics of 3D printing and powder materials used, the oxygen level in both versions of the powder materials was higher than the standard, which is set at less than 0.01%. The powder showed a higher oxygen content, presumably due to oxidation in the air during sampling for chemical analysis. Additionally, Fabrication 2 contains almost no boron, unlike Fabrication 1, for which boron nitride nozzles were used during atomization. It is important to note that boron is highly undesirable in steels for fusion applications, as it can lead to additional helium formation under neutron irradiation. It was found that in both powder material versions, the nickel and copper contents are somewhat higher than required by the specified standard for EUROFER97. Furthermore, the aluminum content in the new Fabrication version was significantly reduced and now complies with the standard, despite being initially similar in the starting materials. Overall, the composition of Fabrication 2 is more favorable than Fabrication 1, both in powder form and after 3D printing, although the content of some elements still does not fully meet the EUROFER97 specification and requires further minor adjustments.

Since argon may have been used during 3D printing and atomization, it was important to determine its content in the 3D-printed material, as high argon concentrations can affect mechanical properties, particularly impact toughness [17,18]. Three measurements of the material from Fabrication 1 showed an argon content of 110 ± 5 ppb, while for Fabrication 2, the

content was 437 ± 102 ppb. This indicates that Fabrication 2 has a significantly higher argon concentration with a more uneven distribution. However, these values remain negligible, suggesting that no significant impact on mechanical properties is expected.

Fig. 3 presents EBSD maps obtained for 3D-printed SLM-EF Fabrication 1 and 2. The maps show the material structure in different orientations: perpendicular (Fig. 3a,b) and parallel (Fig. 3c,d) to the build direction. Overall, the structure closely resembles that of EUROFER97 after the same heat treatment [10,14]. The maps reveal that the material appears highly homogeneous in both directions, with no noticeable texture. However, differences in grain size are observed: in the new Fabrication 2 material, the average martensite packet size is approximately 5.7 µm, whereas in Fabrication 1, it is around 3.8 µm. The differences in grain size between materials produced via SLM for Fabrication 1 and Fabrication 2 are most likely attributed to their chemical composition, as indicated in Table 1, since the printing parameters, hot isostatic pressing conditions, and heat treatment parameters for both Fabrication versions were identical.

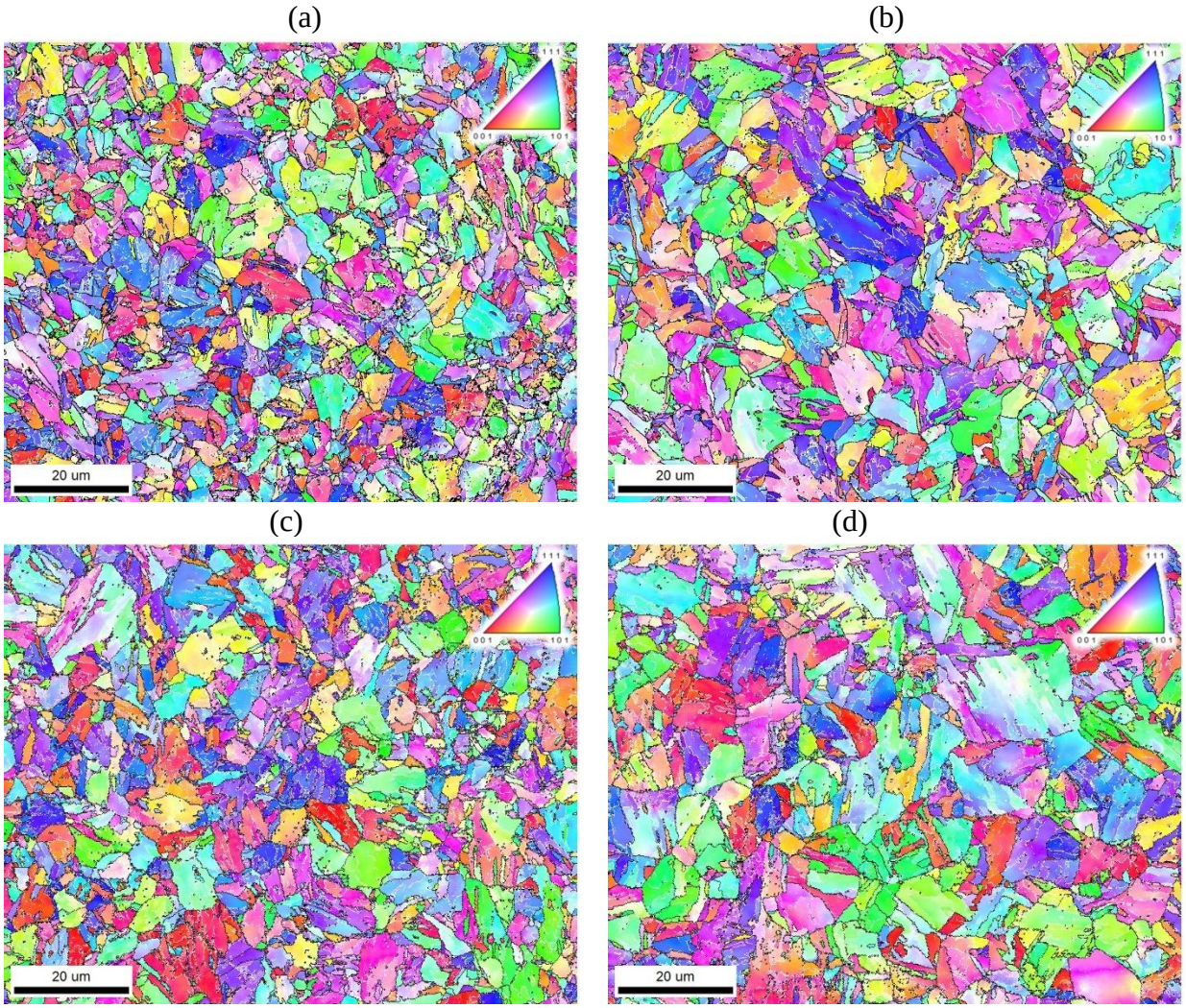


Fig. 3. EBSD maps obtained for 3D printed SLM-EF after HIP and heat treatment: (a, c) Fabrication 1, (b, d) Fabrication 2, (a, b) perpendicular to the build direction, (c, d) parallel to the build direction, with the build direction from top to bottom

Vickers hardness measurements revealed that the hardness of SLM-EF Fabrication 2 after HIP and heat treatment was 213±3 and 217±3 $HV_1$, parallel and perpendicular to the build direction, respectively. This is very close to the hardness value of EUROFER97 after similar treatment (213 HV [12]). In contrast, the hardness of SLM-EF Fabrication 1 was slightly higher, at 241±3 and 242±3 $HV_1$ in the parallel and perpendicular directions, respectively. The differences in hardness are likely again due to minor variations in composition and, consequently, in microstructure.

Tensile testing of the material showed that the yield strength and the ultimate tensile strength for Fabrication 1 and Fabrication 2 SLM-EF in different orientations are nearly identical (Fig. 4). These values are very close to those of the EUROFER97 reference material and exceed the values in the specified standard. As for elongation, the values at room temperature were slightly lower than those for the reference material and specified standard. However, at temperatures of 300°C and 500°C, the elongation values are almost identical to those of the EUROFER97 reference material, and at 700°C, they exceed them. Overall, despite slight differences in chemical composition and microstructure, SLM-EF of both Fabrications exhibited similar strength and ductility properties in tensile tests. In general, they correspond well to the EUROFER97 reference material, demonstrating good reproducibility of mechanical test results across different fabrications.

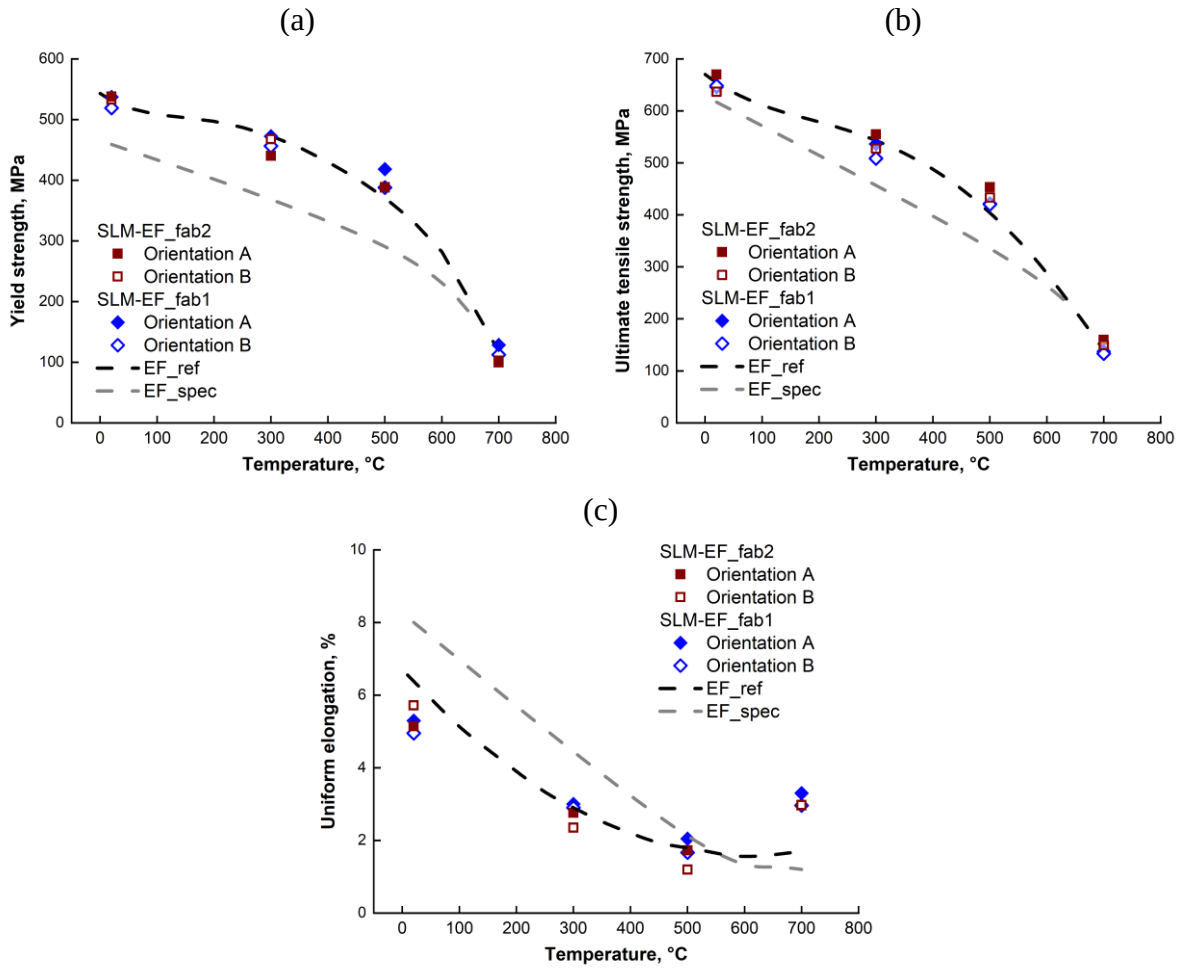


Fig. 4. Tensile test results for SLM-EF from fabrications 1 and 2 at temperatures of 20, 300, 500, and 700°C: (a) yield strength, (b) ultimate tensile strength, and (c) uniform elongation. The materials were evaluated in two orientations: Orientation A, where samples were aligned parallel to the powder layers, and Orientation B, perpendicular to the powder layers. The tensile properties of the reference material EUROFER97 (EF_ref), and data from literature for EF_spec are presented as dashed lines for comparison [12,19–22]. Standard deviations are typically within ±3 % for strength values, ±15 % at 20–300°C, and ±40 % at 500–700°C for elongation.

One of the key and noteworthy results for SLM-EF Fabrication 2 is the Charpy impact toughness test results, shown in Fig. 5. Previous research demonstrated that despite the tensile properties being close to those of EUROFER97 and a similar microstructure, the upper shelf energy (USE) of the 3D-printed material after HIP and heat treatment was found to be roughly 40% lower than that of conventional EUROFER97. Additionally, the ductile-to-brittle transition temperature (DBTT) was shifted by approximately +50°C towards higher temperatures. In contrast, for Fabrication 2, significantly improved results were obtained in similar tests. Notably, the USE slightly exceeded the values for standard EUROFER97 and the reference material. Moreover, the DBTT was lower than that of EUROFER97, with values measured at -120°C for SLM-EF Fabrication 2, compared to -100°C for EUROFER97 and -50°C for Fabrication 1. This demonstrates a remarkable improvement in the impact toughness of SLM-EF Fabrication 2.

Additionally, the Charpy impact tests were performed on specimens oriented both parallel and perpendicular to the build direction, and the results were very close in both orientations. This consistency further confirms the homogeneity of the material, despite the layer-by-layer nature of 3D printing.

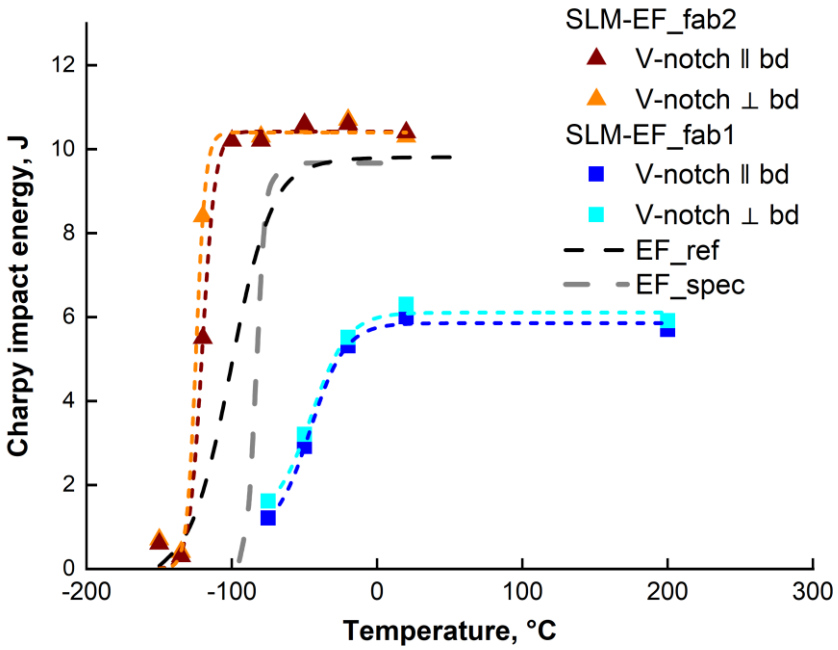


Fig. 5. Charpy impact test results for SLM-EF from Fabrications 1 and 2, tested in two orientations: notch parallel to the build direction (bd) and notch perpendicular to it. Data is fitted with a hyperbolic tangent function (dotted lines). Trend lines for reference material EUROFER97 (EF_ref) and literature data EF_spec are shown as dashed lines [12,19–22].

To understand the reasons behind the significantly improved Charpy impact toughness properties of SLM-EF Fabrication 2 compared to Fabrication 1, microstructural investigations of the fracture surfaces were conducted. Fig. 6 presents the fracture surface microstructures after Charpy impact testing for both Fabrications. Despite a thorough examination of the fracture surfaces, no significant differences were found in the microstructure of the corresponding samples, both in brittle fracture (Fig. 6a,b) and predominantly ductile fracture (Fig. 6c,d). However, it is evident that under the same impact toughness testing conditions at a temperature of -80°C, the SLM-EF Fabrication 1 samples (Fig. 6a) exhibit brittle fracture, while the SLM-EF Fabrication 2 samples show ductile fracture (Fig. 6d).

Since the printing parameters, HIP, and heat treatment were the same, the observed differences in DBTT and USE values between Fabrication 2 and Fabrication 1 can be explained by two key factors: slight differences in chemical composition (due to difference in powder atomization and different plates used), as seen in Table 1, and a somewhat larger grain size for Fabrication 2, as shown in Fig. 3. While smaller grain size is generally associated with improved toughness, it is well known that reducing the effective grain size below a certain threshold (≈1–5 µm) can lead to

decreased plasticity and increased brittleness due to limited dislocation activity [23]. In our case, EBSD-based measurements show that Fabrication 1 has a finer packet structure (≈3.8 µm), whereas Fabrication 2 exhibits a coarser one (≈5.7 µm), which is closer to the reference value for conventionally processed EUROFER97 (≈5.3 µm [14]). Therefore, the coarser microstructure of Fabrication 2 may have contributed positively to the observed Charpy behavior. At the same time, the argon content in the second material is approximately four times higher, but it still appears to be negligible to have any significant effect on the Charpy impact toughness. All these differences, however, do not manifest under relatively slow deformation during tensile testing.

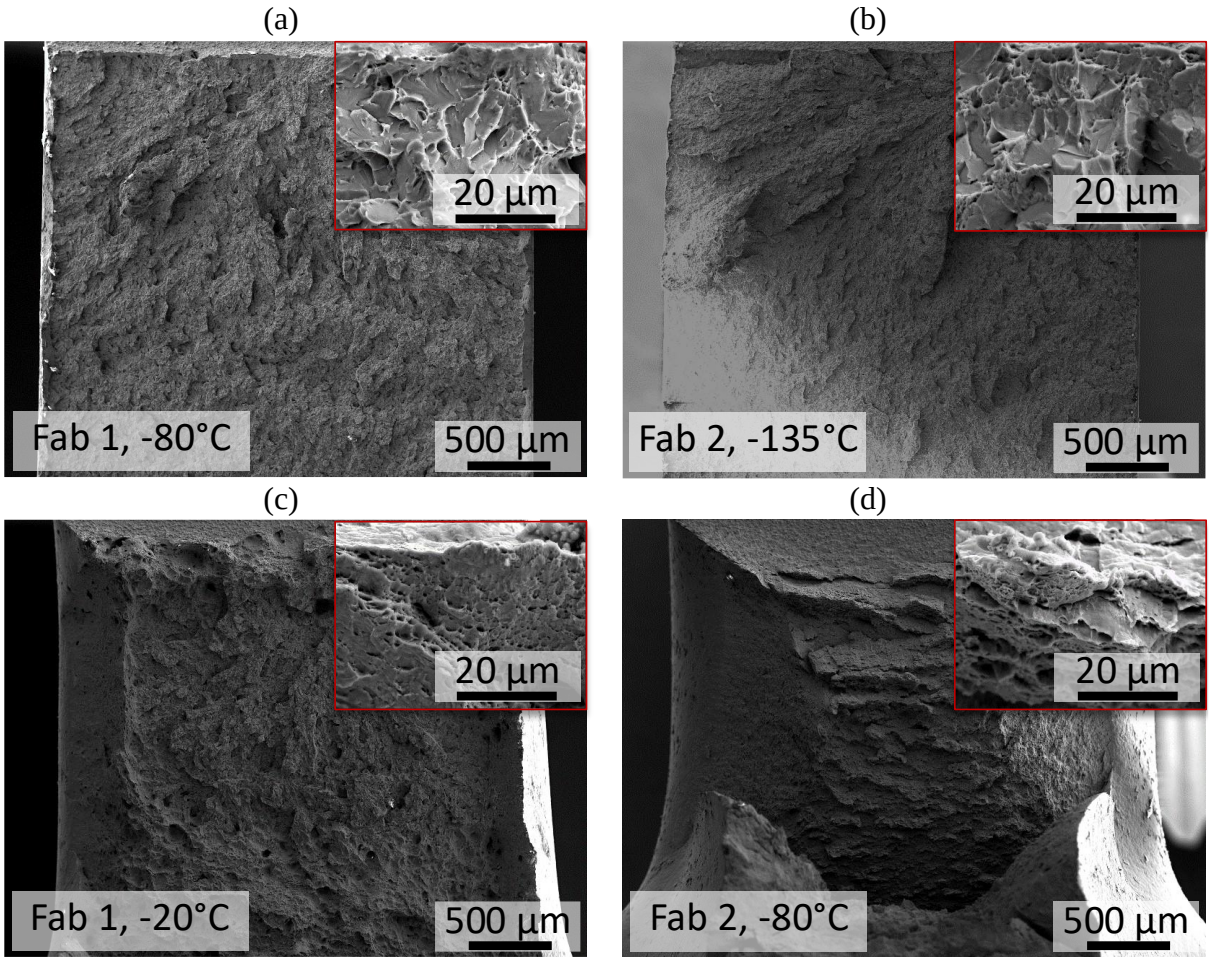


Fig. 6. Microstructure of the fracture surface after Charpy impact tests of SLM-EF samples from (a, c) Fabrication 1 (Fab 1) and (b, d) Fabrication 2 (Fab 2). (a-b) show predominantly brittle fractures, (c-d) exhibit mainly ductile fractures. The test temperature is indicated in the bottom left corner, and the top left corner shows a magnified image near the surface of the V-notch.

### 3.2. SLM-printed capsules

The second part of this study focuses on the SLM-EF components printed using the same technology as for the test blocks shown above. Fig. 7a shows the appearance of a burst capsule in the as-printed condition. Support structures were used at the base of the capsules, designed as

lattice structures to facilitate their removal from the capsules. The surface of the capsules is rough, a characteristic feature of 3D-printed materials.

Some of the capsules were sectioned for microstructural studies in the as-printed condition, while the remaining capsules were subjected to the same post-processing as the blocks in the first part of the study, namely HIP followed by heat treatment. Following these treatments, most of the support structures were removed by lathe machining, and a neck was machined for connection to a Swagelok-type connection for further leak-tightness and burst testing (Fig. 7b). The surface of the capsules slightly darkened after HIP, likely due to residual or impurity gases in the argon atmosphere.

(a)


(b)


Fig. 7. Burst capsules of SLM-EF in the (a) as-printed state and (b) after HIP, heat treatment, and partial lathe processing

Fig. 8a,b illustrate the microstructure of the capsule in cross-sectional and longitudinal views in the as-printed condition. In both sections, protrusions and dimples up to 100 µm in size are visible. Wall thickness measurements showed the following values: for a nominal thickness of 0.5 mm, the actual thickness ranged from 410 to 510 µm; for a nominal thickness of 0.7 mm, it ranged from 540 to 740 µm; and for a nominal thickness of 900 µm, it ranged from 810 to 900 µm. By optimizing the printing parameters, including fine-tuning the outer contour and applying appropriate compensation factors, it should be possible to achieve greater dimensional accuracy and improved surface quality.

The microstructure of the printed material exhibits typical laser scan tracks for this method, forming melt pools approximately 80 µm in size in the cross-section. In the longitudinal section, these melt pools form columnar grains with heights of 100-200 µm. Additionally, as seen in Fig. 8b, remnants of support structures made from the same material are present, but these are finer-grained, likely due to the higher cooling rates at the beginning of the printing process. It is also likely that different printing parameters were used for these elements compared to the bulk

material, as support structures often require modified processing strategies, such as different energy input or melting every second layer.

After HIP and heat treatment, the structure of the capsule completely transformed. It consists of a typical EUROFER97 microstructure after similar treatment, with grain size (distance between high-angle grain boundaries) of approximately 4 µm, consisting of packets of martensitic laths. This value is slightly smaller than that observed in the bulk blocks of Fabrication 2. We attribute this difference to the thinner capsule wall geometry (0.5–0.9 mm), which likely resulted in a faster cooling rate during heat treatment compared to the 10 mm-thick blocks, leading to a modest refinement of the microstructure. The structure was found to be identical in both longitudinal and cross-sectional views (only the cross-sectional view is shown in Fig. 8c). A similar complete transformation of the 3D-printed structure into a homogeneous microstructure was demonstrated in more detail in the previous study [13].

Additionally, a surface layer on the outer surface of the capsule was observed to have larger grains, up to approximately 50 µm in size, in which no martensitic lath packets were present (Fig. 8d). EDS measurements (Fig. 9) revealed that this coarser-grained near-surface region is depleted in both carbon and chromium, forming a layer approximately 30 µm thick. In addition, a thin surface oxide layer, approximately 0.8 µm thick, composed primarily of chromium oxide, was also detected. The presence of this oxide, along with the carbon depletion, suggests that traces of oxygen were present during HIP or subsequent heat treatment, leading to localized surface oxidation and decarburization – a well-known phenomenon in steels under such conditions [24].

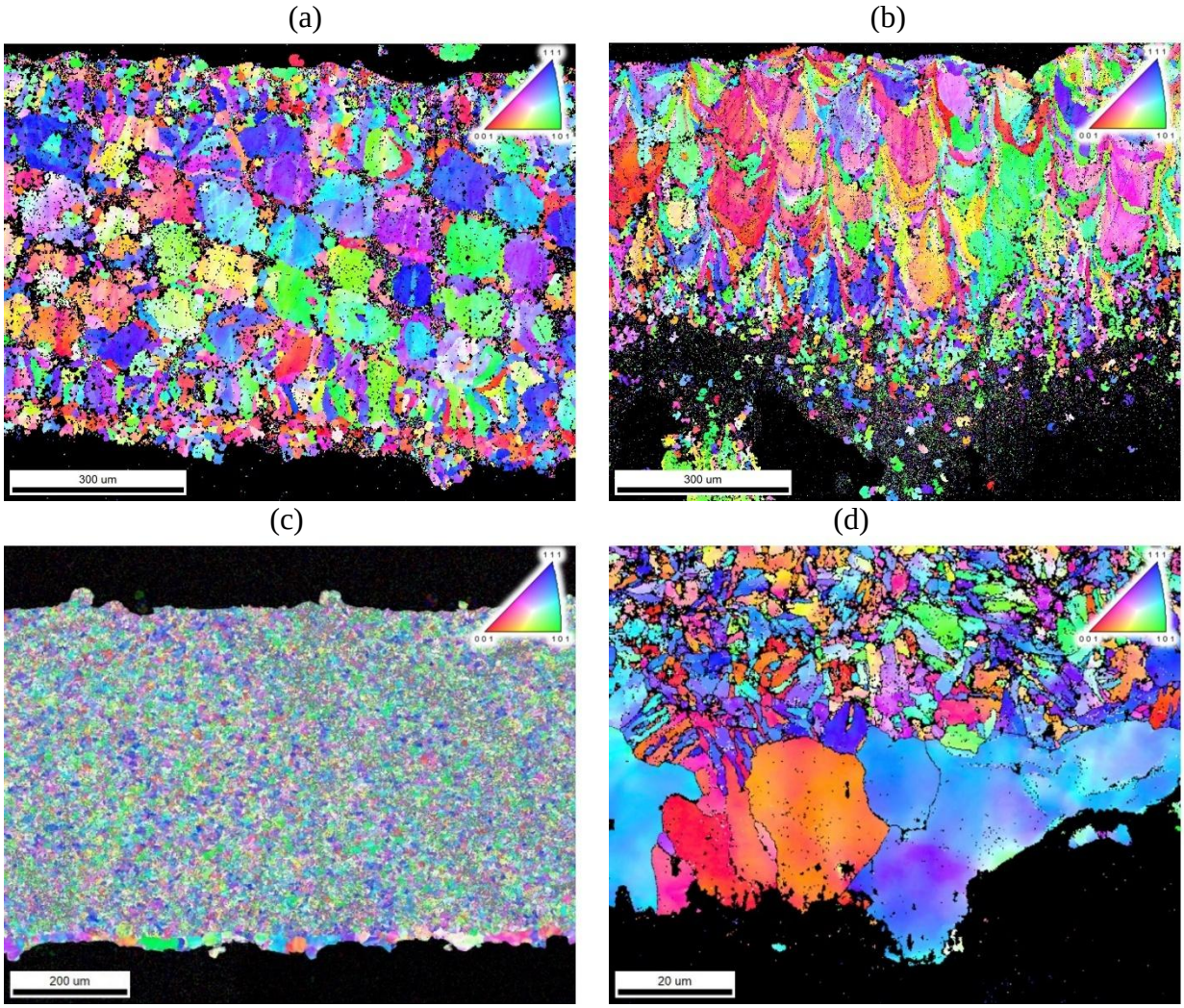


Fig. 8. EBSD maps for burst capsules of SLM-EF with a nominal thickness of 0.7 mm: (a, b) as-printed, (c, d) after HIP and heat treatment. (a, c, d) the plane of the figure coincides with the printing plane, (b) the build direction is from bottom to top. (d) is a magnified image of (c) close to the outer wall of the capsule.

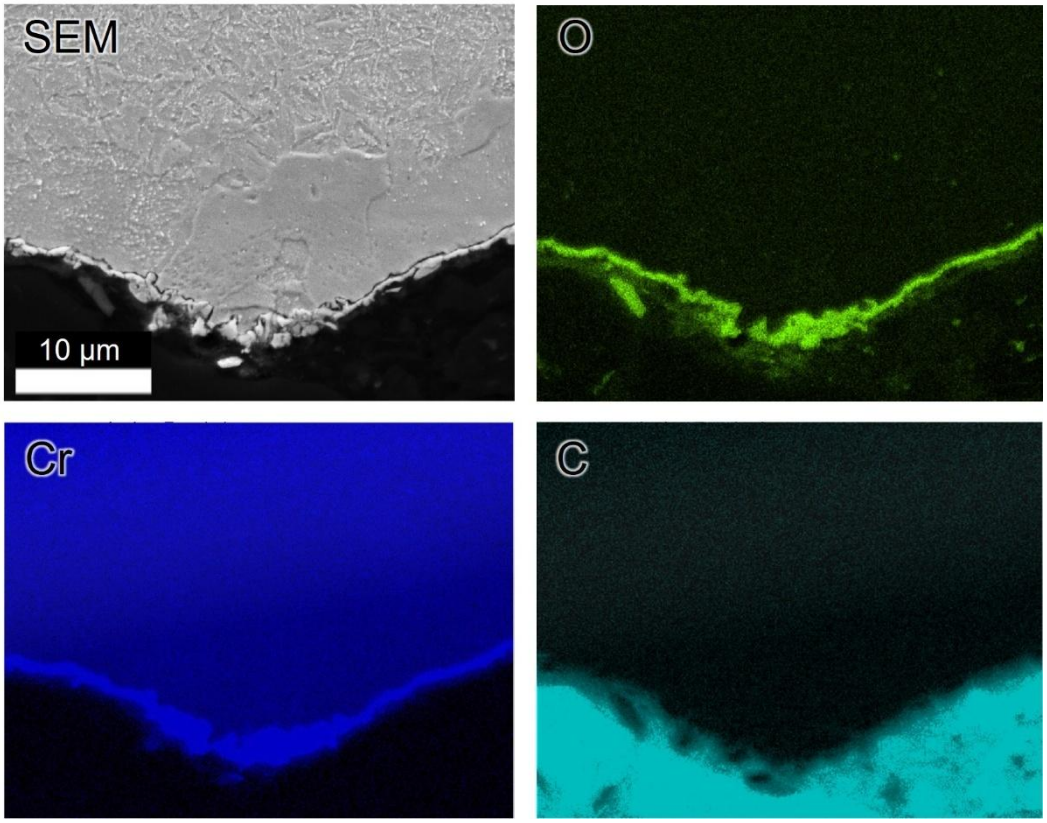


Fig. 9. SEM image and corresponding EDS elemental maps of oxygen, chromium, and carbon in burst capsules of SLM-EF after HIP and heat treatment. The high carbon signal observed in the lower part of the image originates from the conductive mounting resin and should be disregarded.

In the initial phase of testing, all capsules made from SLM-EF were subjected to leak-tightness tests. The test results for capsules with wall thicknesses of 0.5 mm, 0.7 mm, and 0.9 mm are presented in Table 2. It was found that the helium leak rates were less than $7.4 \times 10^{-11}$, $6.7 \times 10^{-11}$, and $6.1 \times 10^{-11}$ Pa·m$^3$/s, respectively. These values are lower than the operating requirements for the ITER torus primary vacuum components or components which become connected to the torus high vacuum (less than $1 \times 10^{-10}$ Pa·m$^3$/s) [25]. Additionally, the measured leak rates are three orders of magnitude below the safety leak rate for vacuum vessel itself (less than $1 \times 10^{-8}$ Pa·m$^3$/s) [25].

Table 2. Results of helium leakage and water burst tests conducted on SLM-EF capsules

| Wall thickness, mm | Leak rate, Pa·m$^3$/s | Ultimate strength, MPa |
|---|---|---|
| 0.5 | $<7.4 \cdot 10^{-11}$ | 708±18 |
| 0.7 | $<6.7 \cdot 10^{-11}$ | 740±6 |
| 0.9 | $<6.1 \cdot 10^{-11}$ | 762±6 |

Fig. 10 shows the appearance of capsules with different thicknesses after burst test. All capsules ruptured longitudinally in the central area. Some capsules exhibit rust-colored, orange-brown stains on the surface, likely resulting from exposure of the deformed samples to water for a few hours at room temperature. This unexpected corrosion behavior warrants further investigation, as EUROFER97 in its as-received condition showed no signs of corrosion even after a week of water immersion.

The ultimate strength of each capsule was determined using the formula $\sigma_{US} = \frac{P \cdot R}{t}$, where $P$ – burst pressure, $R$ – inner radius, $t$ – wall thickness [26,27]. Table 2 provides the average ultimate strength values for capsules of each thickness. Overall, the ultimate strength of the capsules exceeded 700 MPa. According to Fig. 4b, the tensile strength at room temperature for SLM-EF blocks was around 650 MPa at 20°C. The slightly higher strength of the capsules can be explained by the non-uniformity of the capsule wall thickness, as previously shown, which inevitably introduced inaccuracies in the calculations. The consistent behavior of all capsules, with burst pressure increasing proportionally to wall thickness and no capsules failing at significantly lower pressures, indicates the absence of major local defects in the production process. This uniform performance confirms the reliability and reproducibility of the SLM fabrication method.


Fig. 10. Appearance of SLM-EF capsules after water burst testing. The left row has a nominal wall thickness of 0.5 mm, the middle 0.7 mm, and the right 0.9 mm.

## 4. Conclusions

This study investigated the selective laser melting of EUROFER97 powder, with a detailed examination of two fabrications and their structural features, tensile behavior, impact toughness, and leak-tightness relevant for fusion applications. The results confirm the potential of SLM technology to produce EUROFER97 components with properties comparable to or even surpassing those of conventionally manufactured materials.

The use of a different EUROFER97 starting plates and modification of the powder preparation method resulted in a more favorable chemical composition and slightly larger grain size (≈5.7 µm vs. ≈3.8 µm). These improvements contributed to superior Charpy impact toughness, with an

upper shelf energy exceeding the EUROFER97 standard and a lower ductile-to-brittle transition temperature (-120°C vs. -100°C for EUROFER97). Additionally, the tensile properties, including yield strength, ultimate tensile strength, and elongation, were very close to those of the EUROFER97 reference material.

Capsules printed using SLM demonstrated excellent leak-tightness, with helium leak rates significantly below the requirements for ITER torus vacuum components. Burst tests confirmed an ultimate strength exceeding 700 MPa at room temperature. The successful printing and post-processing of capsules and blocks indicate that SLM can be effectively applied to complex geometries, such as thin-walled structures and intricate components for fusion reactor blankets. This opens opportunities for complicated designs with tailored mechanical properties.

## CRediT authorship contribution statement

**R. Gaisin**: Investigation, Writing - Original Draft, Writing - Review & Editing, Visualization, Methodology. **C. Bonnekoh:** Investigation, Methodology, Writing - Review & Editing. **S. Bonk**: Investigation, Methodology, Conceptualization, Writing - Review & Editing, **H. Neuberger**: Investigation, Conceptualization, Writing - Review & Editing. **V. Chakin:** Investigation, Methodology, Writing - Review & Editing. **M. Rieth**: Writing - Review & Editing, Funding acquisition.

## Acknowledgements

This work has been carried out within the framework of the EUROfusion Consortium, funded by the European Union via the Euratom Research and Training Programme (Grant Agreement No 101052200 — EUROfusion). Views and opinions expressed are however those of the author(s) only and do not necessarily reflect those of the European Union or the European Commission. Neither the European Union nor the European Commission can be held responsible for them.

The authors would like to express their gratitude to Rosswag GmbH for performing the selective laser melting and to NANOVAL GmbH for the atomization of powders. Special thanks are extended to T. Bergfeldt, KIT IAM-AWP, for conducting the chemical analyses, and to R. Ziegler, U. Jäntsch, S. Baumgärtner, and D. Bolich, KIT IAM-AWP, for their assistance in sample preparation and mechanical testing. The authors greatly appreciate Dr. David Malmström (Swerim AB, Sweden) for his support in measuring the argon content. The authors also thank U. Fuhrmann and R. Heger, KIT ITEP, for conducting helium leakage tests, as well as S. Fischer, KIT TEC, for performing the burst tests.

## References

[1] C.Y. Yap, C.K. Chua, Z.L. Dong, Z.H. Liu, D.Q. Zhang, L.E. Loh, S.L. Sing, Review of selective laser melting: Materials and applications, Applied Physics Reviews 2 (2015) 041101. https://doi.org/10.1063/1.4935926.

[2] B. Zhang, Y. Li, Q. Bai, Defect Formation Mechanisms in Selective Laser Melting: A Review, Chin. J. Mech. Eng. 30 (2017) 515–527. https://doi.org/10.1007/s10033-017-0121-5.

[3] S.L. Sing, W.Y. Yeong, F.E. Wiria, B.Y. Tay, Z. Zhao, L. Zhao, Z. Tian, S. Yang, Direct selective laser sintering and melting of ceramics: a review, RPJ 23 (2017) 611–623. https://doi.org/10.1108/RPJ-11-2015-0178.

[4] I.A. Pelevin, A.Yu. Nalivaiko, D.Yu. Ozherelkov, A.S. Shinkaryov, S.V. Chernyshikhin, A.N. Arnautov, S.V. Zmanovsky, A.A. Gromov, Selective Laser Melting of Al-Based Matrix Composites with Al2O3 Reinforcement: Features and Advantages, Materials 14 (2021) 2648. https://doi.org/10.3390/ma14102648.
[5] H. Neuberger, F. Hernandez, J. Rey, S. Bonk, M. Rieth, J. Koch, B. Schmalisch, O. Müller, K.-U. Volker, D. Volker, S. Leyh, R. Niewöhner, A. Brenner, Fabrication of HCPB breeding blanket components using the additive manufacturing processes of selective laser melting and cold spray, Fusion Engineering and Design 160 (2020) 112026. https://doi.org/10.1016/j.fusengdes.2020.112026.
[6] H. Neuberger, J. Rey, M. Hees, E. Materna-Morris, D. Bolich, J. Aktaa, A. Meier, S. Fischer, C. Schorle, U. Fuhrmann, R. Heger, I. Dlouhý, L. Stratil, B. Kloetzer, Selective Laser Sintering as Manufacturing Process for the Realization of Complex Nuclear Fusion and High Heat Flux Components, Fusion Science and Technology 72 (2017) 667–672. https://doi.org/10.1080/15361055.2017.1350521.
[7] C. Koehly, H. Neuberger, L. Bühler, Fabrication of thin-walled fusion blanket components like flow channel inserts by selective laser melting, Fusion Engineering and Design 143 (2019) 171–179. https://doi.org/10.1016/j.fusengdes.2019.03.184.
[8] M. Klimenkov, U. Jäntsch, M. Rieth, A. Möslang, Correlation of microstructural and mechanical properties of neutron irradiated EUROFER97 steel, Journal of Nuclear Materials 538 (2020) 152231. https://doi.org/10.1016/j.jnucmat.2020.152231.
[9] A. Zinovev, C.-C. Chang, J. Van Eyken, E. Gaganidze, D. Terentyev, Effect of neutron irradiation to 0.7 and 1.4 dpa on the tensile mechanical properties and microstructure of EUROFER97 steel, (2023). https://doi.org/10.5445/IR/1000158322.
[10] M. Duerrschnabel, U. Jäntsch, R. Gaisin, M. Rieth, Microstructural insights into EUROFER97 batch 3 steels, Nuclear Materials and Energy 35 (2023) 101445. https://doi.org/10.1016/j.nme.2023.101445.
[11] M. Duerrschnabel, E. Gaisina, R. Gaisin, M. Walter, J. Aktaa, M. Rieth, Nanoscale insights into the corrosion of EUROFER by lithium ceramics, Corrosion Science 199 (2022) 110190. https://doi.org/10.1016/j.corsci.2022.110190.
[12] M. Rieth, M. Schirra, A. Falkenstein, P. Graf, S. Heger, H. Kempe, R. Lindau, H. Zimmermann, EUROFER 97. Tensile, charpy, creep and structural tests, Karlsruhe, 2003. https://doi.org/10.5445/IR/270055720.
[13] S. Bonk, H. Neuberger, D. Beckers, J. Koch, S. Antusch, M. Rieth, Additive manufacturing technologies for EUROFER97 components, Journal of Nuclear Materials 548 (2021) 152859. https://doi.org/10.1016/j.jnucmat.2021.152859.
[14] S. Bonk, M. Dürrschnabel, H. Neuberger, E. Simondon, M. Rieth, Microstructural features in additively manufactured EUROFER97 components, Fusion Engineering and Design 173 (2021) 112813. https://doi.org/10.1016/j.fusengdes.2021.112813.
[15] J. Hoffmann, M. Rieth, M. Klimenkov, S. Baumgärtner, Improvement of EUROFER's mechanical properties by optimized chemical compositions and thermo-mechanical treatments, Nuclear Materials and Energy 16 (2018) 88–94. https://doi.org/10.1016/j.nme.2018.05.028.
[16] Grant Deliverable MAT D25.15. Materials Properties Handbook: 2nd formal release, EUROfusion Consortium, MAT-Project, 2017.
[17] M. Cheng, J. Wu, Z.-G. Lu, R.-P. Guo, L. Xu, R. Yang, Effect of Argon-Induced Porosity on Mechanical Properties of Powder Metallurgy Titanium Alloy Components using Hot

Isostatic Pressing, Acta Metall. Sin. (Engl. Lett.) 34 (2021) 1386–1394. https://doi.org/10.1007/s40195-021-01243-z.
[18] M. Klimiankou, R. Lindau, A. Möslang, Energy-filtered TEM imaging and EELS study of ODS particles and Argon-filled cavities in ferritic–martensitic steels, Micron 36 (2005) 1–8. https://doi.org/10.1016/j.micron.2004.08.001.
[19] A. Alamo, J.L. Bertin, V.K. Shamardin, P. Wident, Mechanical properties of 9Cr martensitic steels and ODS-FeCr alloys after neutron irradiation at 325°C up to 42dpa, Journal of Nuclear Materials 367–370 (2007) 54–59. https://doi.org/10.1016/j.jnucmat.2007.03.166.
[20] E. Lucon, R. Chaouadi, M. Decréton, Mechanical properties of the European reference RAFM steel (EUROFER97) before and after irradiation at 300 °C, Journal of Nuclear Materials 329–333 (2004) 1078–1082. https://doi.org/10.1016/j.jnucmat.2004.04.023.
[21] J. Henry, X. Averty, A. Alamo, Tensile and impact properties of 9Cr tempered martensitic steels and ODS-FeCr alloys irradiated in a fast reactor at 325°C up to 78dpa, Journal of Nuclear Materials 417 (2011) 99–103. https://doi.org/10.1016/j.jnucmat.2010.12.203.
[22] E. Materna-Morris, A. Möslang, H.-C. Schneider, Tensile and low cycle fatigue properties of EUROFER97-steel after 16.3dpa neutron irradiation at 523, 623 and 723K, Journal of Nuclear Materials 442 (2013) S62–S66. https://doi.org/10.1016/j.jnucmat.2013.03.038.
[23] Y. Wang, C. Huang, X. Ma, J. Zhao, F. Guo, X. Fang, Y. Zhu, Y. Wei, The optimum grain size for strength-ductility combination in metals, International Journal of Plasticity 164 (2023) 103574. https://doi.org/10.1016/j.ijplas.2023.103574.
[24] H.D. Alvarenga, T.V. De Putte, N. Van Steenberge, J. Sietsma, H. Terryn, Influence of Carbide Morphology and Microstructure on the Kinetics of Superficial Decarburization of C-Mn Steels, Metall Mater Trans A 46 (2015) 123–133. https://doi.org/10.1007/s11661-014-2600-y.
[25] Robert Pearce, Liam Worth, ITER Technical report. ITER Vacuum Handbook, 2019.
[26] D.R. Moss, Pressure vessel design manual: illustrated procedures for solving major pressure vessel design problems, 3rd ed, Gulf Professional Pub, Amsterdam ; Boston, 2004.
[27] C.T. Herakovich, Thin-Walled Pressure Vessels, in: A Concise Introduction to Elastic Solids, Springer International Publishing, Cham, 2017: pp. 77–81. https://doi.org/10.1007/978-3-319-45602-7_13.